symmetry

MDPI

Article

Defect Detection inside a Rail Head by Ultrasonic Guided Waves

Jingsong Xie [1,2], Wenxiang Ding [3,*], Wen Zou [2], Tiantian Wang [2] and Jinsong Yang [2]

[1] State Key Laboratory of Traction Power, Southwest Jiaotong University, Chengdu 610031, China
[2] School of Traffic and Transportation Engineering, Central South University, Changsha 410083, China
[3] School of Mechanical and Electrical Engineering, Shenzhen Polytechnic, Shenzhen 518055, China
* Correspondence: wenxiangding@szpt.edu.cn

Abstract: Early detection of defects inside a rail is of great significance to ensure the safety of rail transit. This work investigated the ability of ultrasonic guided waves (UGWs) to detect internal defects in a rail head. First, the model of UGW propagation in rail, which has an irregular cross-section, was constructed based on the semi-analytical finite element (SAFE) method. Fundamental characteristics, such as wavenumber, phase or group velocity, and wave structure inside the rail, were then calculated. Following modal and vibration energy distribution analysis, a guided wave mode that is sensitive to transverse fissure (TF) defects was selected, and its excitation method was proposed. The effectiveness of the excitation method was confirmed by simulations performed in the ABAQUS software. According to the simulation data, the dispersion curve calculated by using the two-dimensional Fourier fast transform (2D-FFT) coincided well with that of the SAFE method. After that, the sensitivity of the selected mode to internal rail defects was validated and its ability to locate defects was also demonstrated. Finally, the effects of excitation frequency, defect size, and vertical and horizontal defect depth on the reflection waveforms were investigated.

Keywords: ultrasonic guided waves; finite element methods; transverse fissure defect; rail inspection

check for updates

Citation: Xie, J.; Ding, W.; Zou, W.; Wang, T.; Yang, J. Defect Detection inside a Rail Head by Ultrasonic Guided Waves. *Symmetry* **2022**, *14*, 2566. https://doi.org/10.3390/sym14122566

Academic Editor: Fei Gao

Received: 13 November 2022
Accepted: 29 November 2022
Published: 5 December 2022

1. Introduction

Acting as one of the most important national infrastructures, railways across the world are developing rapidly to reach higher speeds and carry more passengers and loads. Early detection of defects in a rail is essential to ensure train safety as small defects may lead to rail breakage, which can cause serious accidents and economic losses [1,2]. According to the Central Organization for Railway Electrification (CORE) safety overview in the years 2009–2015, 803 accidents happened on the Indian railway, resulting in 620 deaths and 1855 injuries [3]. A total of 47% of these accidents were caused by the derailment of trains and most of them were due to undetected cracks.

The defects in rails can be divided into three categories: (a) defects originating from the rail manufacturing process, such as transverse fissures; (b) defects arising because of inappropriate use or installation, such as surface spalling caused by wheelburn; (c) defects due to rail wear and fatigue, such as corrugation, head checking, and squats [4–6]. Among these defects, transverse fissures (TFs), which originate from a nucleus inside the rail head and are enlarged progressively by vehicle dynamic loads, have been considered as the first cause of rail breakage [7]. A TF spreads outwards in the form of a round or oval surface that is substantially at a right angle to the length of the rail, and its propagation speed is greatly enlarged when it reaches a size of 20–25% of the rail cross-section [7]. To avoid railway accidents, various non-destructive evaluation (NDE) techniques have been developed to inspect defects in rails, including visual inspection, magnetic flux leakage (MFL), eddy currents (ECs), ultrasonics, and ultrasonic guided wave (UGW) techniques [4,6,8]. A visual inspection can be implemented by a human expert or video cameras. The test speed can be as high as a train's speed but only defects on the visible outer surface of the rail can be detected. The MFL and EC methods are suitable for surface and near-surface defect detection. The presence of a defect will produce a disturbance to the electromagnetic field or magnetic flux. Their promotion of use is limited by the sensitivity to the lift-off distance from the test specimens [6]. Conventional ultrasonics are the most common techniques used in industry. A total of 7–9 ultrasound transducers refracted at 0°, 37°, or 45° and 70° angles were mounted within a liquid-filled tire to scan the specimens. The inspection speed varied from 40 km/h to 80 km/h [4]. This method was more accurate, however, its use in near-surface defect detection was restricted due to the strong reflection of the surface [9]. Compared to other methods, the UGW technique has been shown to be more efficient and is widely used in many applications due to its long-distance propagation, wide coverage of the waveguide cross-section, and sensitivity to small defects [10,11]. The interactions between UGWs and railhead surface cracks, with or without shelling, were studied by Rose [12,13] and Bartoli [14,15]. Certain UGW modes can also be optimally excited to detect defects in the rail web [16,17] and rail feet [2,18,19]. However, there has been little research on the interaction of UGWs with internal rail defects. Compared to surface defects, the internal defects of a rail head are more dangerous, and they are not occasionally found [20].

In this work, the feasibility of the UGW technique to detect internal defects in a rail head after manufacturing was explored. Firstly, a modal analysis based on wave structure data calculated by the semi-analytical finite element (SAFE) method was performed. A guided wave mode, which is sensitive to internal rail defects, was selected and its excitation method was presumed. Secondly, UGW propagation was simulated in the ABAQUS finite element (FE) software. Comparison between the results of FE simulation and the SAFE method showed that the excitation method proposed is effective. A single mode sensitive to internal rail defects could be excited. Finally, the interaction between UGWs and transverse fissures was investigated.

2. Modeling of UGW Propagation and Its Interaction with Defects

In this section, a brief description of the SAFE method and three-dimensional (3D) FE modeling with ABAQUS software is provided.

2.1. SAFE Method

The SAFE method has shown great efficiency and accuracy in modeling wave propagation in waveguides of arbitrary cross-sections, especially for complex ones such as rail [10,21,22]. Only the cross-section of the waveguide needs to be discretized with finite elements and the wave propagation along the axial direction is represented by harmonic motion. As shown in Figure 1, the CHN60 rail of China railway is considered in this work, which has a density of 7830 kg/m^3, a Young modulus of 210 gPa, and a Poisson's ratio of 0.3. The cross-section was discretized by 598 four-node quadrilateral elements to ensure sufficient accuracy at high frequencies (Figure 1b).

The displacement in the z-axis is assumed harmonic and thus the displacement field (u_x, u_y, u_z) can be expressed as

$$u(x,y,z,t) = \begin{bmatrix} u_x(x,y,z,t) \\ u_y(x,y,z,t) \\ u_z(x,y,z,t) \end{bmatrix} = \begin{bmatrix} U_x(x,y) \\ U_y(x,y) \\ U_z(x,y) \end{bmatrix} e^{i(\xi z - \omega t)} \tag{1}$$

where ξ and ω are the wavenumber and angle frequency, respectively, and i is the imaginary part.

Based on the virtual work principle and the assembly of finite element matrices, the general wave equation for free vibration can be obtained as

$$\left[\mathbf{K}_1 + i\xi\mathbf{K}_2 + \xi^2\mathbf{K}_3 - \omega^2\mathbf{M}\right]_N \mathbf{U} = 0 \tag{2}$$

where $\mathbf{K}_1$, $\mathbf{K}_2$, and $\mathbf{K}_3$ are the stiffness matrices, $\mathbf{M}$ is the mass matrix, the subscript N is the number of degrees of freedom, and $\mathbf{U}$ is the nodal displacement vector.

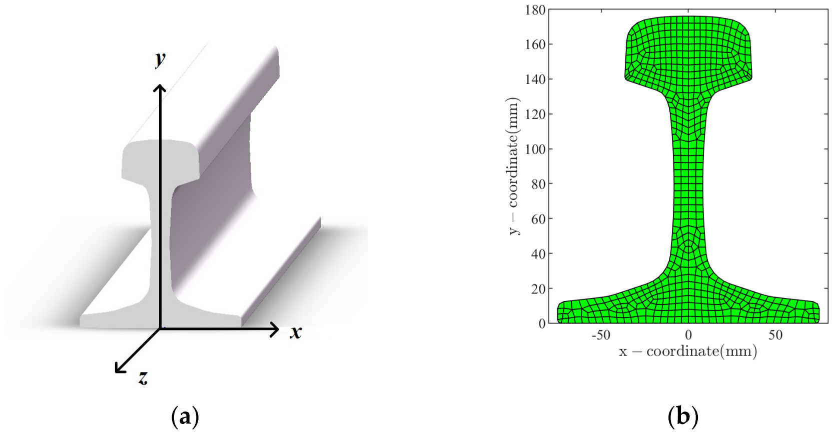

Figure 1. Schematic diagram of the CHN60 rail: (**a**) coordinate system; (**b**) discretization of the cross-section with four-node quadrilateral elements.

Solving the eigenvalue problem of Equation (2), the dispersion relation between wavenumber ξ and frequency ω can be directly obtained. Subsequently, according to their definitions, phase velocity $c_p = \omega/\xi$ and group velocity $c_g = \partial\omega/\partial\xi$ are calculated. The eigenvector **U** in Equation (2) represents the displacements of all nodes of the cross-section and thus mode shape for each vibration mode can be depicted. More details on the description and derivation of the SAFE method can be found in [10,21].

2.2. FE Modeling with ABAQUS

To investigate the interaction of UGWs with arbitrarily shaped defects, the SAFE method mentioned above is not enough and traditional FE modeling is required. A global–local or hybrid SAFE–FE approach has also been proposed recently to deal with this problem [23–25]. In this work, 3D FE analysis was performed with the commercial software ABAQUS/Explicit for studying the wave propagation and scattering effects in rails.

2.2.1. Wave Propagation

A CHN60 rail of 2 m with the same material properties as mentioned in Section 2.1 was considered and created in ABAQUS, as shown in Figure 2a.

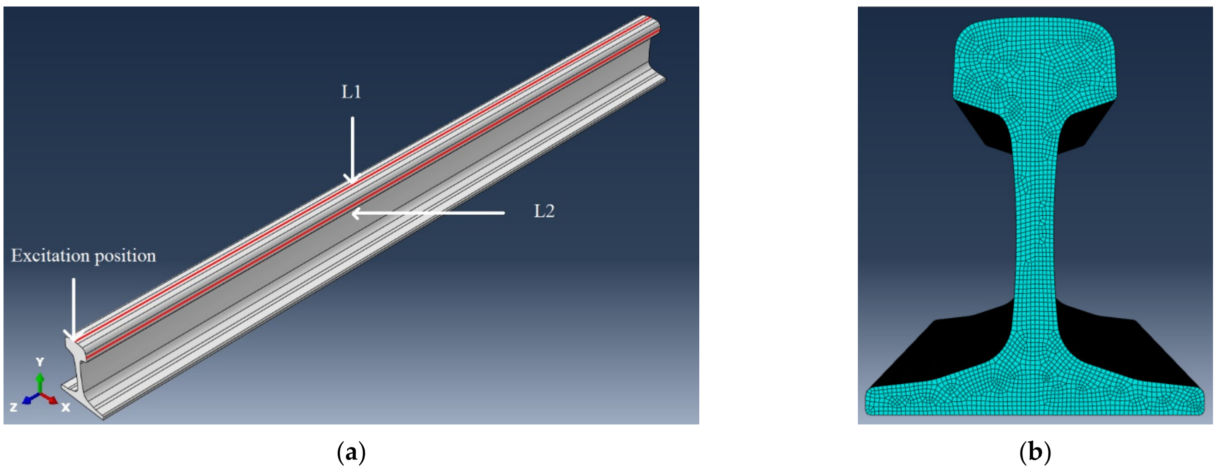

Figure 2. CHN60 rail model in ABAQUS: (**a**) whole geometry; (**b**) front view after meshing.

The numerical stability and accuracy of ABAQUS/Explicit dynamic analysis depend mainly on two factors: temporal and spatial resolution. For a good spatial resolution l_e, it is a good rule of thumb to use 10 elements per shortest wavelength [14,26,27], that is

$$l_e \le \lambda_{min}/10 \tag{3}$$

The determination of the integration time step Δt is recommended as follows [14]

$$\Delta t \le 1/20 f_{max} \text{ and } \Delta t \le l_{min}/c_L \tag{4}$$

where f_{max} is the maximum frequency of the analysis, l_{min} is the smallest dimension of the finite elements, and c_L is the longitudinal wave velocity.

In this work, the maximum frequency f_{max} considered was 150 kHz, consequently, the global element size was set to 2 mm and the time increment was fixed at 10^{-8} s. For an intact case, the whole rail model was shaped with 2,271,000 linear hexahedral elements of type C3D8R, and Figure 2b shows its front view after meshing. Except for a narrowband, 5-cycle Hanning-windowed toneburst was applied at one end and the rail was assumed stress-free. The center frequency (f_c) of the excitation varied from 50 kHz to 125 kHz. In the field output request, stresses and displacements were selected as output variables with 50 evenly spaced time intervals. In the history output request, displacements of the 1001 nodes at intervals of 2 mm on the top center line (L1 in Figure 2a) and gage/field side (L2 in Figure 2a) of the rail head were produced in the database. After completion of the module setting, a job was created and submitted for analysis. The results were written to the output database.

2.2.2. Wave Scattering from Internal Defects

To study the wave scattering effect of UGWs, transverse fissures (TFs), which are the primary cause of rail breakage, are considered here. Their growth is normally slow, to a size of 20–25%, and a nucleus of more than 3/8 in (around 9.5 mm) can be identified after breaking [28,29]. Based on these, a TF defect was modeled with a cross-section in the form of an ellipse and located 500 mm from the excitation end (Figure 3a). The vertical depth of a TF beneath the top center surface is denoted by d_1 (Figure 3b) and varied from 2 to 16 mm. The horizontal depth beneath the gage/field surface is specified by a parameter d_2 (Figure 3b) and varied from 2 to 10 mm. The width of a TF, determined by the semi-major axis h (Figure 3b), also varied from 6 to 16 mm. The aspect ratio of the ellipse, i.e., the ratio between the minor axis and the major axis, was fixed to 0.75. The extent of a TF defect along the longitudinal axis z was 2 mm, which is equal to the global mesh size. The pulse–echo technique was used here to locate defects, and two sensors (red dots in Figure 3a) were installed on the surfaces of the top center head and gage/field side, respectively.

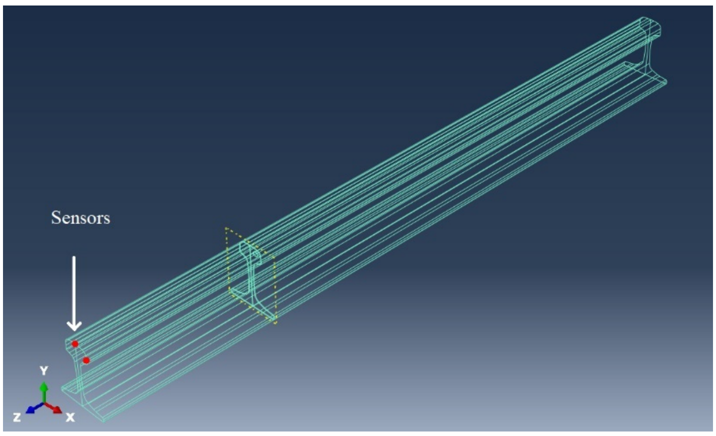

(**a**)

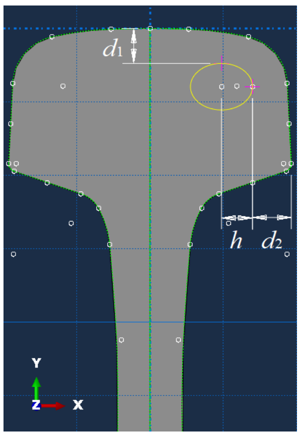

(**b**)

Figure 3. Three-dimensional (3D) modeling of a transverse fissure (TF) defect in a rail head: (**a**) longitudinal location; (**b**) dimension and position in the cross-section.

3. Mode Selection and Verification

3.1. Mode Selection and Excitation Based on the SAFE Method

Using the SAFE method, the wavenumber and group velocity dispersion curves for the CHN60 rail were calculated between 0.1 kHz and 100 kHz, and the results are shown in Figure 4. We can see that the number of vibration modes increased significantly with increasing frequency. The multi-mode and dispersion characteristics make UGW-based defect detection challenging. To eliminate, or at least reduce, the influence of these, specific excitation methods have been investigated by a host of researchers [30–32]. However, the excitation method proposed in [32] for rails is a bit too idealistic. Firstly, node-type excitation is not very feasible due to the certain size of the transducer. Secondly, the excitation of each specific mode always requires four to five nodes distributed at different locations on the rail surface, which also makes the excitation system complex.

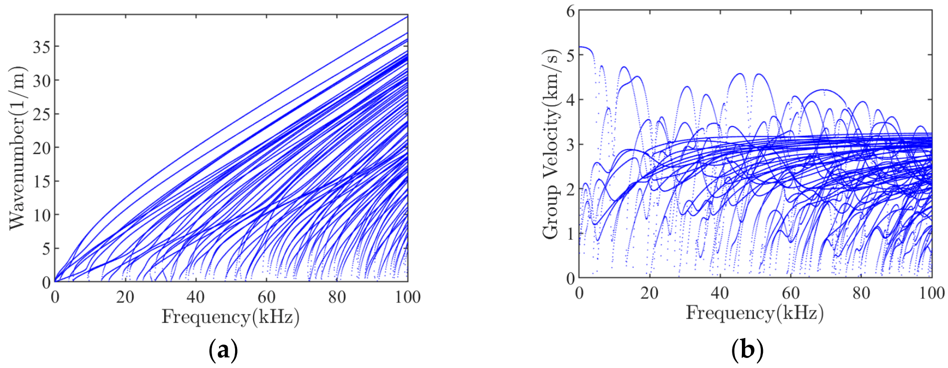

Figure 4. Dispersion curves for the CHN60 rail by the SAFE method: (**a**) wavenumber vs. frequency; (**b**) group velocity vs. frequency.

To select suitable modes for TF defect detection, a modal analysis based on the SAFE method was carried out first. The vibration energy of the rail head (E_{head}) is defined as

$$E_{head} = \sum_{i=1}^{M}\left(u_{xi}^2 + u_{yi}^2 + u_{zi}^2\right) \; and \; z_i > 127.5\,mm \tag{5}$$

where M is the number of nodes belonging to the rail head. Then, the energy ratio (ER) is as follows

$$ER = \frac{E_{head}}{E_{rail}} \tag{6}$$

where E_{rail} is the vibration energy of all nodes in the rail cross-section.

Figure 5 shows the wavenumber and group velocity dispersion curves for CHN60 expressed by ER. Since only symmetric modes were excited in our study, the dispersion curves of the anti-symmetric modes were erased from the figures. Shading on each dot linearly changed from green to red in the range of $0 \leq ER \leq 1$. Mode shapes of three modes at 50 kHz, S1, S3 and S6, are plotted in Figure 6, respectively. As we can see, the vibration of mode S1 was mainly concentrated on the rail foot. It was not suitable for the detection of defects in the rail head. In contrast, the vibrations of modes S3 and S6 were mainly focused on the rail head and their ER values were 0.99 and 0.98, respectively. Mode S3 was a good candidate for the detection of surface cracks, while mode S6 was more sensitive to internal defects, such as TF.

Theoretically, if a load distribution equivalent to one mode shape is applied to the cross-section, including excitation nodes, directions, and amplitudes, only this single mode will be excited. As a result, line loads of around 20 mm on the surfaces of the top center head (case I) and the gage/field side (case II) were applied to excitation modes S3 and S6, respectively, as shown in Figure 7.

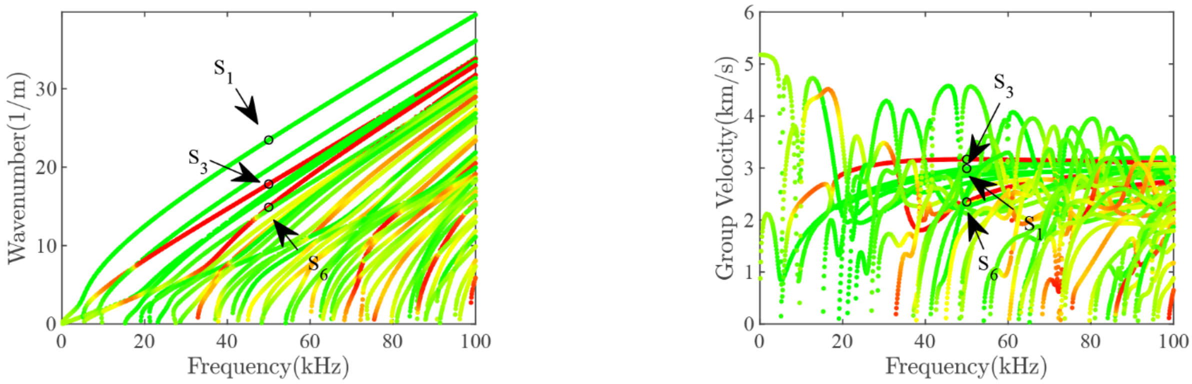

(**a**) (**b**)

Figure 5. Dispersion curves for the CHN60 rail expressed by the ER: (**a**) wavenumber vs. frequency; (**b**) group velocity vs. frequency.

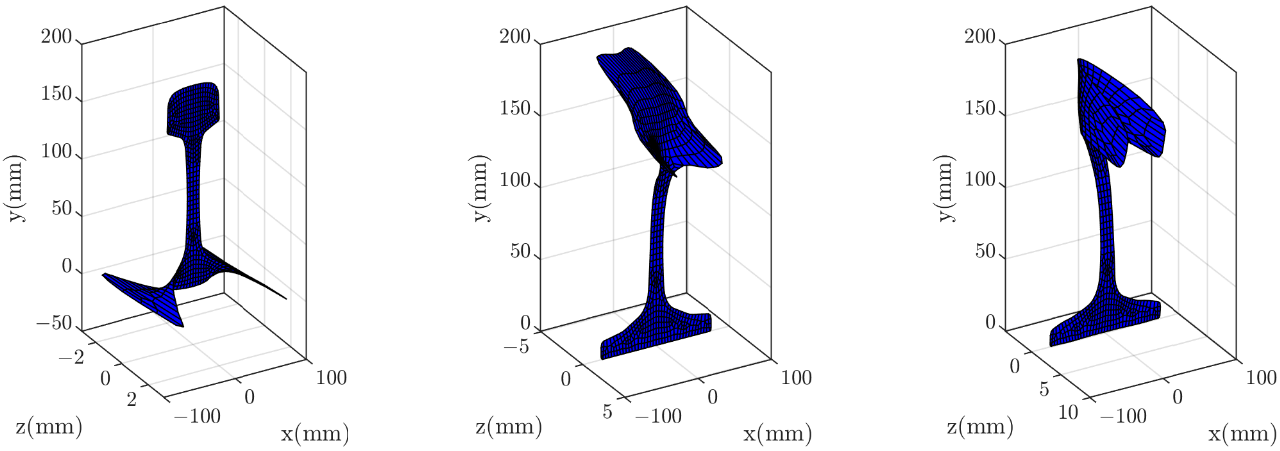

(**a**) (**b**) (**c**)

Figure 6. Mode shapes of three vibration modes at 50 kHz: (**a**) S1; (**b**) S3; (**c**) S6.

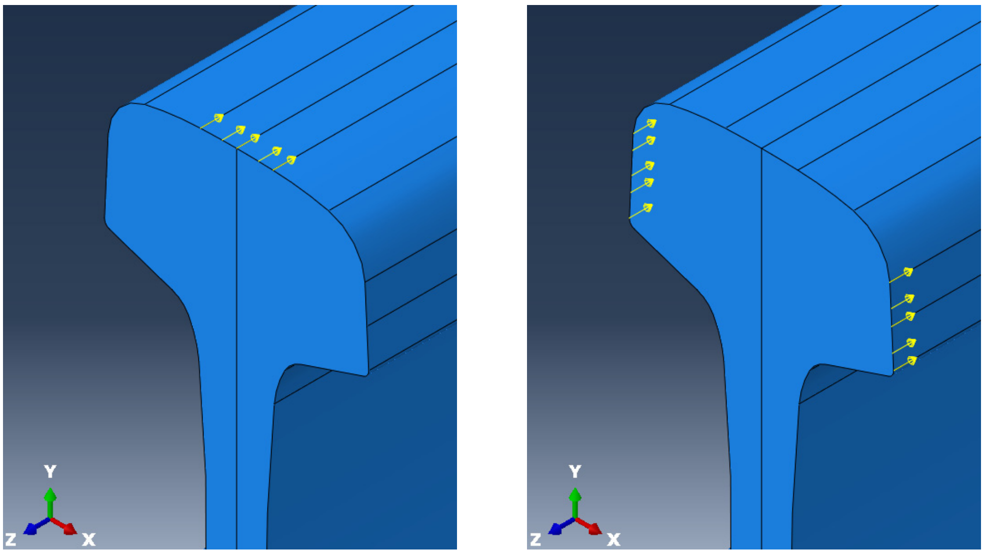

(**a**) (**b**)

Figure 7. Excitation methods of modes S3 (**a**) and S6 (**b**).

3.2. Mode Verification

The two-dimensional fast Fourier transform (2D-FFT) was used to analyze the displacements of the 1001 nodes on the L1 or L2 lines. Figure 8a shows that in case I, not only mode S3 but also another dominant mode, S9, was excited. However, in case II (Figure 8b), the wave propagation was only dominated by mode S6. This was also well illustrated in the waterfall plots of the displacements (Figure 8c–f). UGWs were highly dispersed at 50 kHz, particularly in the S6 mode (Figure 8d), and it was also difficult to identify the two dominant modes in case I (Figure 8c). At a higher frequency of 75 kHz, these vibration modes had a much smaller dispersion and could be easily identified. It was proven that line loads on surfaces of the rail gage/field side (case II) were effective for exciting the S6 mode and could be used for the detection of TF defects in rail heads.

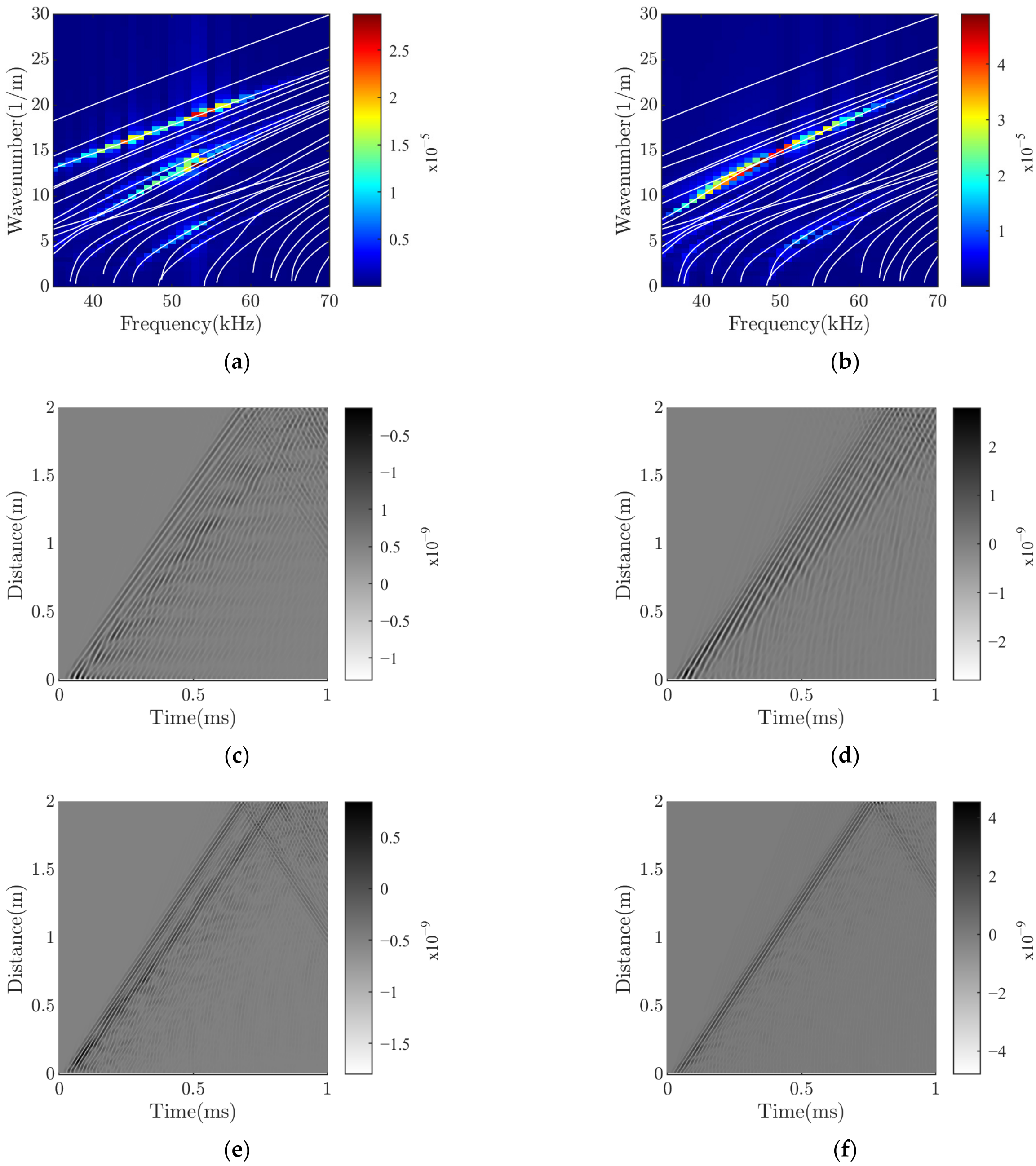

Figure 8. Frequency vs. wavenumber dispersion curves and waterfall plots of displacements: 2D-FFT results of case I (**a**) and case II (**b**) loading; waterfall plots of case I (**c**) and case II (**d**) at 50 kHz; waterfall plots of case I (**e**) and case II (**f**) at 75 kHz.

4. Detection of Internal Rail Defects Using UGWs

4.1. Defect Localization

Figure 9 shows displacements generated by the two excitation methods in Section 3.1. TF defects with dimensions of d_1 = 6 mm, d_2 = 6 mm, and h = 16 mm were considered here. It can be observed in Figure 9a that after interaction with a TF defect, a reflection echo at around t = 0.35 ms was generated. According to Figure 5b, the wave speed v of mode S6 at 75 kHz was 2827.8 m/s, so the damage location could be calculated by $vt/2$ and was expected to be 494.9 mm from the excitation point. Since the actual distance was 500 mm, the predicted value gave an error of only 5.1 mm (1%). Figure 9b indicates that the pulse-echo test on the surface of the top center head was not sensitive to internal defects. No reflection echo of mode S3 or S9 could be detected.

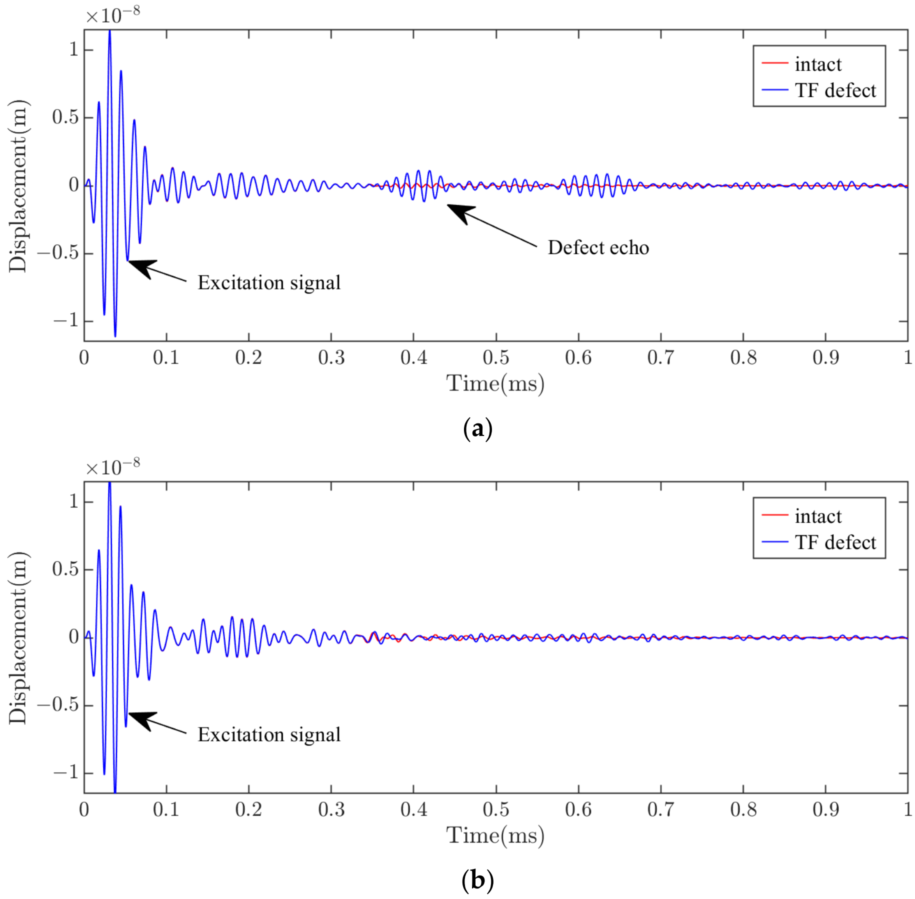

Figure 9. Pulse-echo displacements of UGWs with 75 kHz of excitation loaded on: (**a**) the top center surface; (**b**) the gage/field side surface.

Two static frames of mode S6 during wave propagation and after interaction with the TF defect are shown in Figure 10. A y-plane view cut was created in the center of the TF defect to expose the internal features. Just as the wave structure in Figure 6c indicated, the vibration energy of mode S6 was mainly concentrated on the two horizontal sides of the rail head, making it sensitive to internal defects.

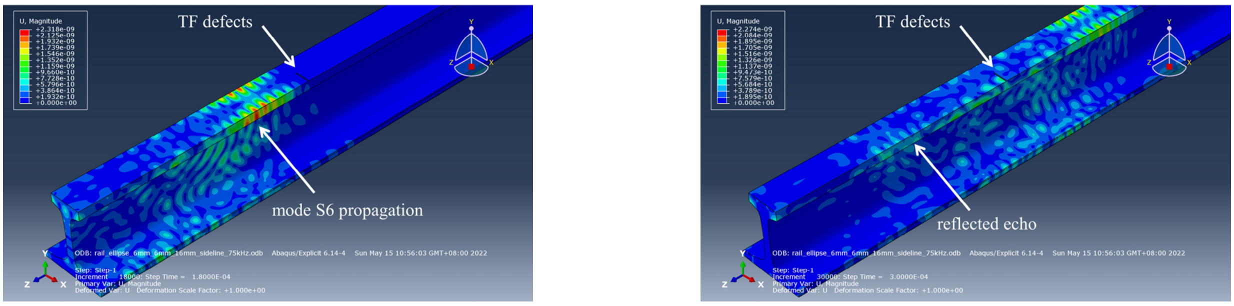

(**a**) (**b**)

Figure 10. UGW propagation and scattering pattern of 75 kHz: (**a**) the frame at 0.18 ms; (**b**) the frame at 0.3 ms.

4.2. Effect of Excitation Frequency

Figure 11 shows pulse-echo displacements for the excitation of different center frequencies. The waveforms were tailored between 0.3 and 0.6 ms to focus on the reflection echoes. For 50 kHz, there was no obvious reflection echo of the TF defect. This might be in part due to the large wavelength of mode S6 at 50 kHz (around 46 mm). For higher frequencies, the reflected echo appeared, and the TF defect could be characterized. However, as the excitation frequency increased from 75 kHz to 125 kHz, the amplitudes of the reflected echoes decreased and some interference modes were excited, leading to the complexity of the waveform. To maintain a balance between its sensitivity to defects and the influence of multi-modes, an excitation frequency of 75 kHz is recommended.

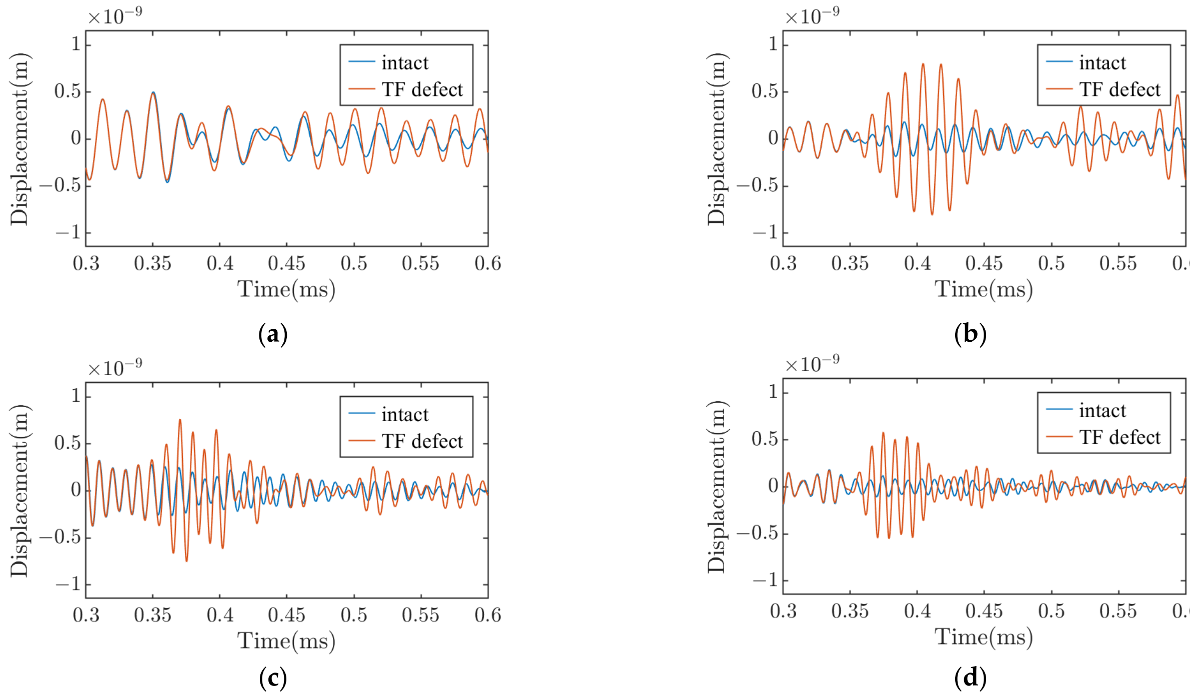

Figure 11. Pulse-echo displacement of UGWs at different center frequency excitation: (**a**) 50 kHz; (**b**) 75 kHz; (**c**) 100 kHz; (**d**) 125 kHz.

4.3. Effect of Defect Size

In this part, the dependence of reflection echo amplitude on the defect size was investigated. The defect depth was kept constant to $d_1 = d_2 = 6$ mm. Figure 12a shows the displacement waveforms. We can see that the reflected echo became stronger as the defect size increased from 8 mm to 16 mm. The reflection coefficient α_r was introduced and is defined as the ratio of the amplitude of the reflected echo A_{echo} to that of the excitation signal $A_{excitation}$.

$$\alpha_r = \frac{A_{echo}}{A_{excitation}} \tag{7}$$

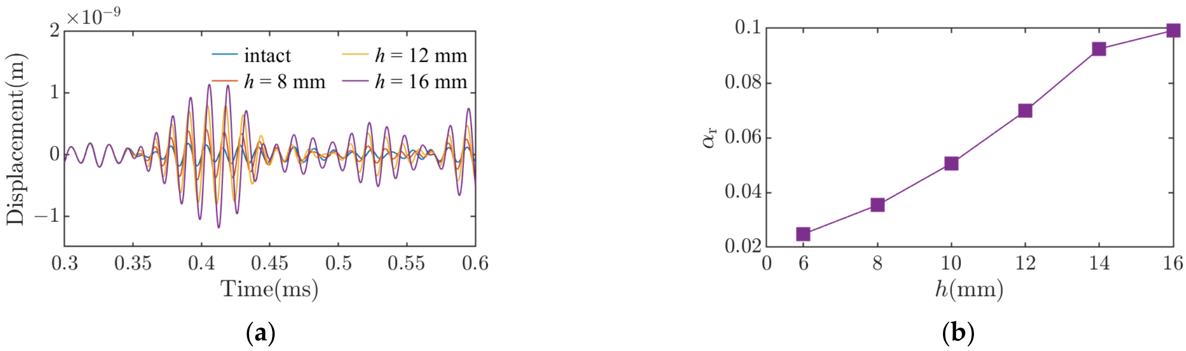

Figure 12. Amplitude of the reflected echo, depending on the size h of the defect (d_1 = d_2 = 6 mm): (**a**) displacement signals; (**b**) reflection coefficient α_r vs. h.

As shown in Figure 12b, the bigger the defect size, the larger the reflection coefficient α_r. The reflection coefficient α_r monotonically increased with increasing h, from 0.025 of the defect size scale at h = 6 mm to 0.1 at h = 16 mm.

4.4. Effect of Defect Depth

Figure 13 illustrates the dependence of the reflection echo amplitude on the vertical depth d_1 of the defect. The amplitude of the echo waveform in Figure 13a varied very little with the vertical depth. Using the same y-axis limits as in Figure 12b, the variation pattern of reflection coefficient (Figure 13b) was close to flat, with a minimum value of 0.06 and a maximum value of 0.07. Another way of saying this is that the sensitivity of mode S6 to the internal defect detection was not affected by the vertical depth.

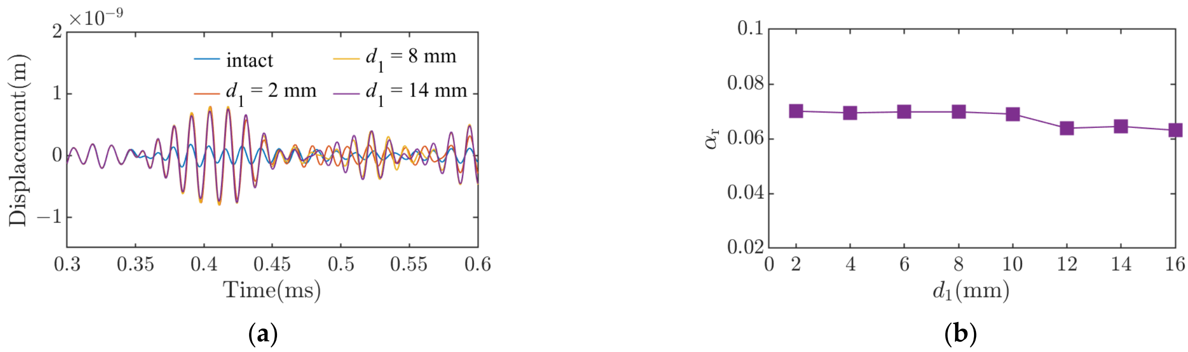

Figure 13. Amplitude of the reflected echo, depending on the vertical depth d_1 of defect (d_2 = 6 mm, h = 12 mm): (**a**) displacement signals; (**b**) reflection coefficient α_r vs. d_1.

Similarly, the effect of horizontal depth d_2 on the amplitude of a reflected echo was also investigated and the result is shown in Figure 14a. It could be observed that, horizontally, the deeper the defect, the weaker the echoes were that it reflected on the surface. Figure 14b shows that the reflection coefficient α_r decreased monotonically with increasing horizontal depth d_2, from 0.09 of the defect size depth at d_2 = 2 mm to 0.05 at d_2 = 10 mm.

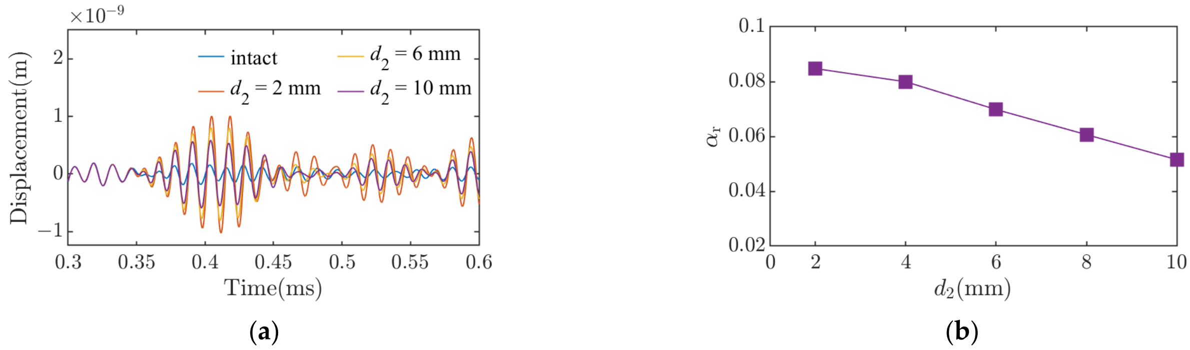

Figure 14. Amplitude of the reflected echo, depending on the horizontal depth d_2 of defect (d_1 = 6 mm, h = 12 mm): (**a**) displacement signals; (**b**) reflection coefficient α_r vs. d_2.

5. Conclusions

The early detection of internal rail defects is important to ensure the safety of rail transit, and there has not been much research on the interaction between ultrasonic guided waves (UGWs) and internal rail defects. In this work, finite element simulations were carried out to investigate the ability of UGWs to detect transverse fissures (TFs) in rail heads after manufacturing. This systematic research could also be applied to rails in operation. Based on the results of our study, the following findings have been obtained:

1. Following modal and energy distribution analysis, a symmetric mode S6 was selected and recommended for the detection of TF defects.
2. An excitation method, i.e., line loads on surfaces of the rail gage and field sides, was proposed to excite mode S6 and its effectiveness was proven. The dispersion curve calculated by using a two-dimensional Fourier fast transform (2D-FFT) shows that wave propagation was dominated by mode S6 and was close to 'single' mode. Meanwhile, its localization ability was also confirmed.
3. Line loads on the surface of the center head excited two dominant modes, S3 and S9. The pulse-echo test on the top center head suggested that they were not good for internal defect detection.
4. To maintain a balance between its sensitivity to defects and the influence of multi-modes, an excitation frequency at 75 kHz is recommended.
5. The reflection coefficients of defects were found to increase and decrease monotonically with increasing defect size and horizontal depth, respectively. It is not affected much by the vertical depth of the defect.

These findings suggest that symmetric mode S6 is a good candidate for the early detection of defects inside rail heads. The experimental verification of these findings will be undertaken as our future work. Contact loading using rectangular piezoelectric ceramic and contactless loading such as laser or air-coupled ultrasonic transducers will be conducted to excite the S6 mode on the gage/field side. Meanwhile, ellipse-shaped holes of different sizes will also be cut in the rail head.

Author Contributions: All the authors J.X., W.D., W.Z., T.W. and J.Y. worked together in the conceptualization, methodology, and validation of the results presented here. W.D. and W.Z. performed the modeling and simulation. J.X. and W.D. were responsible for the writing of the paper. T.W. and J.Y. collaborated in the revision of the manuscript. All authors have read and agreed to the published version of the manuscript.

Funding: This work was supported by the Joint Funds of the National Natural Science Foundation of China, grant number U2268205, the Natural Science Foundation of Hunan Province China, grant number 2021JJ40765, the Open Project of State Key Laboratory, grant number TPL2109, and the Stable Support Plan for Colleges and Universities in Shenzhen, grant number 20220812171109001.

Data Availability Statement: The datasets used and/or analyzed during the current study are available from the corresponding author on reasonable request.

Conflicts of Interest: The authors declare no conflict of interest.

References

1. Alahakoon, S.; Sun, Y.Q.; Spiryagin, M.; Cole, C. Rail Flaw Detection Technologies for Safer, Reliable Transportation: A Review. *J. Dyn. Syst. Meas. Control* **2017**, *140*, 020801. [CrossRef]
2. Pathak, M.; Alahakoon, S.; Spiryagin, M.; Cole, C. Rail Foot Flaw Detection Based on a Laser Induced Ultrasonic Guided Wave Method. *Measurement* **2019**, *148*, 106922. [CrossRef]
3. Vishesh, S.; Srinath, M.; Sreeram, S.; Jayanth, P.; Bharadwaj, D.D.S.; Venkatachalapathi, S.S. Advanced Monitoring of Rail Cracks Using LASER-EMAT System. *IJARCCE* **2016**, *5*, 413–416. [CrossRef]
4. Papaelias, M.P.; Roberts, C.; Davis, C.L. A Review on Non-Destructive Evaluation of Rails: State-of-the-Art and Future Development. *Proc. Inst. Mech. Eng. Part F J. Rail Rapid Transit* **2008**, *222*, 367–384. [CrossRef]
5. Cannon, D.F.; Edel, K.-O.; Grassie, S.L.; Sawley, K. Rail Defects: An Overview. *Fatigue Fract. Eng. Mater. Struct.* **2003**, *26*, 865–886. [CrossRef]
6. Bombarda, D.; Vitetta, G.M.; Ferrante, G. Rail Diagnostics Based on Ultrasonic Guided Waves: An Overview. *Appl. Sci.* **2021**, *11*, 1071. [CrossRef]
7. Masmoudi, M.; Yaacoubi, S.; Koabaz, M.; Akrout, M.; Skaiky, A. On the Use of Ultrasonic Guided Waves for the Health Monitoring of Rails. *Proc. Inst. Mech. Eng. Part F J. Rail Rapid Transit* **2021**, *236*, 469–489. [CrossRef]
8. Antipov, A.G.; Markov, A.A. Detectability of Rail Defects by Magnetic Flux Leakage Method. *Russ. J. Nondestruct. Test.* **2019**, *55*, 277–285. [CrossRef]
9. Zhu, Q.; Zhang, Y.; Zhang, H.; Memoli, G. Ultrasonic Inspection of near Surface Defects with Additive Manufactured Metasurface Lens. *Front. Mater.* **2022**, *9*, 1025518. [CrossRef]
10. Bartoli, I.; Marzani, A.; di Scalea, F.L.; Viola, E. Modeling Wave Propagation in Damped Waveguides of Arbitrary Cross-Section. *J. Sound Vib.* **2006**, *295*, 685–707. [CrossRef]
11. Xing, B.; Yu, Z.; Xu, X.; Zhu, L.; Shi, H. Research on a Rail Defect Location Method Based on a Single Mode Extraction Algorithm. *Appl. Sci.* **2019**, *9*, 1107. [CrossRef]
12. Rose, J.L.; Avioli, M.J.; Mudge, P.; Sanderson, R. Guided Wave Inspection Potential of Defects in Rail. *NDT & E Int.* **2004**, *37*, 153–161. [CrossRef]
13. Lee, C.M.; Rose, J.L.; Cho, Y. A Guided Wave Approach to Defect Detection under Shelling in Rail. *NDT & E Int.* **2009**, *42*, 174–180. [CrossRef]
14. Bartoli, I.; di Scalea, F.L.; Fateh, M.; Viola, E. Modeling Guided Wave Propagation with Application to the Long-Range Defect Detection in Railroad Tracks. *NDT & E Int.* **2005**, *38*, 325–334. [CrossRef]
15. Coccia, S.; Bartoli, I.; Marzani, A.; di Scalea, F.L.; Salamone, S.; Fateh, M. Numerical and Experimental Study of Guided Waves for Detection of Defects in the Rail Head. *NDT & E Int.* **2011**, *44*, 93–100. [CrossRef]
16. Ramatlo, D.A.; Wilke, D.N.; Loveday, P.W. Development of an Optimal Piezoelectric Transducer to Excite Guided Waves in a Rail Web. *NDT & E Int.* **2018**, *95*, 72–81. [CrossRef]
17. Wu, J.; Tang, Z.; Lv, F.; Yang, K.; Yun, C.B.; Duan, Y. Ultrasonic Guided Wave-Based Switch Rail Monitoring Using Independent Component Analysis. *Meas. Sci. Technol.* **2018**, *29*, 115102. [CrossRef]
18. Moustakidis, S.; Kappatos, V.; Karlsson, P.; Selcuk, C.; Gan, T.-H.; Hrissagis, K. An Intelligent Methodology for Railways Monitoring Using Ultrasonic Guided Waves. *J. Nondestruct. Eval.* **2014**, *33*, 694–710. [CrossRef]
19. Yue, G.; Cui, X.; Zhang, K.; Wang, Z.; An, D. Guided Wave Propagation for Monitoring the Rail Base. *Math. Probl. Eng.* **2020**, *2020*, 4756574. [CrossRef]
20. Han, S.-W.; Cho, S.-H.; Jang, G.-W.; Park, J.-H. Non-Contact Inspection of Rail Surface and Internal Defects Based on Electromagnetic Ultrasonic Transducers. *J. Intell. Mater. Syst. Struct.* **2015**, *27*, 427–434. [CrossRef]
21. Hayashi, T.; Song, W.-J.; Rose, J.L. Guided Wave Dispersion Curves for a Bar with an Arbitrary Cross-Section, a Rod and Rail Example. *Ultrasonics* **2003**, *41*, 175–183. [CrossRef] [PubMed]
22. Andhavarapu, E.V.; Loveday, P.; Long, C.S.; Heyns, P. Accuracy of Semi-Analytical Finite Elements for Modelling Wave Propagation in Rails. In Proceedings of the Seventh South African Conference on Computational and Applied Mechanics (SACAM10), Pretoria, South Africa, 10–13 January 2010.
23. Srivastava, A.; di Scalea, F.L. Quantitative Structural Health Monitoring by Ultrasonic Guided Waves. *J. Eng. Mech.* **2010**, *136*, 937–944. [CrossRef]
24. Long, C.S.; Loveday, P.W. Validation of Hybrid SAFE-FE Guided Wave Scattering Predictions in Rail. In *AIP Conference Proceedings*; AIP Publishing LLC: New York, NY, USA, 2015.
25. Spada, A.; Capriotti, M.; di Scalea, F.L. Global-Local Model for Guided Wave Scattering Problems with Application to Defect Characterization in Built-up Composite Structures. *Int. J. Solids Struct.* **2020**, *182–183*, 267–280. [CrossRef]
26. Alleyne, D.; Cawley, P. A Two-Dimensional Fourier Transform Method for the Measurement of Propagating Multimode Signals. *J. Acoust. Soc. Am.* **1991**, *89*, 1159–1168. [CrossRef]
27. Masoumi, M.; Giles, R.K. Analysis of Wave Scattering in Pipes with Non-Axisymmetric and Inclined Angle Defects Using Finite Element Modeling. *Int. J. Appl. Mech.* **2021**, *13*, 2150012. [CrossRef]

28. Duffy, M.C. The Standard Rail Section, Transverse Fissures and Reformed Mill Practice, 1911–1955. *J. Mech. Work. Technol.* **1980**, *4*, 285–305. [CrossRef]
29. Danbury, C. *Rail Defects Manual*; Sperry Rail Service: New York, NY, USA, 1964.
30. Xu, B.; Giurgiutiu, V. Single Mode Tuning Effects on Lamb Wave Time Reversal with Piezoelectric Wafer Active Sensors for Structural Health Monitoring. *J. Nondestruct. Eval.* **2007**, *26*, 123–134. [CrossRef]
31. Borigo, C.; Rose, J.L.; Yan, F. A Spacing Compensation Factor for the Optimization of Guided Wave Annular Array Transducers. *J. Acoust. Soc. Am.* **2013**, *133*, 127–135. [CrossRef]
32. Xining, X.; Lu, Z.; Bo, X.; Zujun, Y.; Liqiang, Z. An Ultrasonic Guided Wave Mode Excitation Method in Rails. *IEEE Access* **2018**, *6*, 60414–60428. [CrossRef]